

Scattering Curves of Ordered Mesoscopic Materials

S. Förster,* A. Timmann, M. Konrad, C. Schellbach, and A. Meyer

Institut für Physikalische Chemie, Universität Hamburg, Grindelallee 117, D-20146 Hamburg, Germany

S. S. Funari

HASYLAB, DESY, Notkestrasse 85, D-22603 Hamburg, Germany

P. Mulvaney

School of Chemistry, University of Melbourne, Parkville, VIC 3010 Australia

R. Knott

ANSTO, Menai, NSW 2234 Australia

Received: July 22, 2004; In Final Form: October 22, 2004

Analytical expressions for the scattering functions of ordered mesoscopic materials are derived and compared to experimentally determined scattering curves. Ordered structures comprising spheres (fcc, bcc, hcp, sc), cylinders (hex, sq), and lamellar structures are considered. The expressions take into account particle size distributions and lattice point deviations, domain size, core/shell structures, as well as peak shapes varying analytically between Lorentzian and Gaussian functions. The expressions allow one to quantitatively describe high-resolution synchrotron small-angle X-ray (SAXS) and neutron scattering (SANS) curves from lipid and block copolymer lyotropic phases, core/shell nanoparticle superstructures, ordered nanocomposites, and ordered mesoporous materials. In addition, the diffuse out-of-plane scattering of grazing incidence GISAXS and GISANS experiments of laterally ordered thin films can be quantitatively analyzed.

1. Introduction

Many substances such as surfactants, lipids, block copolymers, nanoparticles, polymer colloids, and biopolymers can self-assemble into ordered mesoscopic superstructures, i.e., structures on length scales of 1–1000 nm. Such nanostructured materials are not only fascinating in their own right but are also of great importance in biomedical applications, catalysis, photonics, and high-performance materials.^{1–4}

Among the analytical techniques that are most widely used to characterize ordered mesoscopic materials are optical and electron microscopy, X-ray and neutron diffraction, and spectroscopic methods such as NMR and IR. With the advent of modern X-ray optics in sealed tube or rotating anode X-ray devices, and with the use of high-brilliance synchrotron-SAXS and SANS beamlines, high-resolution scattering curves over a large q -range can now be obtained within short accumulation times (down to milliseconds), enabling a fast and detailed measurement and analysis of ordered mesoscopic materials over the complete size range of 1 nm up to several μm . The amount of available information that could be obtained from these scattering curves can go considerably beyond the simple determination of peak positions and peak widths.

For a quantitative analysis of X-ray or neutron scattering curves, methods have been developed for ordered lattices of spheres using particle distribution functions^{5–8} and paracrystal theory,^{9,10} and for lamellae and bilayers using interfacial distribution functions¹¹ or the Caillé model.^{12–14} These models consider the influence of particle size, volume fraction, and degree of order to calculate the scattering curves. For many applications it would be desirable to have a common approach

that allows one to calculate scattering curves of the most prevalent ordered spherical (bcc, fcc, hcp, sc), cylindrical (sq, hex), and lamellar structures (lam) in order to obtain complete information on the space group, unit cell dimension, mean lattice displacement, particle size and size distribution, core/shell structure, and mean domain size. A general framework for such an approach has been given by Ruland.^{15,16} Within this framework, and together with the approach we developed for the calculation of particle form factors,¹⁷ we outline a general approach based on the decoupling approximation that yields analytical expressions for the scattering curves of ordered d -dimensional structures, where $d = 1$ for disks or lamellae, $d = 2$ for cylinders, and $d = 3$ for spherical structures. We discuss advantages and limitations of the model and demonstrate, using examples from literature and our own experiments, the applicability of this model to quantitatively fit high-resolution SAXS and SANS curves of core/shell nanoparticle superlayers, surfactant, lipid and block copolymer lyotropic phases, as well as ordered nanocomposites, mesoporous materials, and nanostructured thin films.

2. Experimental Section

2.1. Samples. The block copolymers, poly(butadiene-*b*-ethylene oxide) (PB-PEO) and poly(isoprene-*b*-ethylene oxide) (PI-PEO), were synthesized by living anionic polymerization and have narrow molecular weight distribution. The synthesis is described elsewhere.¹⁸ Their degrees of polymerization (subscripts) and sample code are PB₄₃-PEO₅₉-16, PI₉₂-PEO₃₄-2, PI₉₃-PEO₈₇-3, and PI₅₈-PEO₁₃₁-11 as determined from mass spectrometry (MALDI-TOF-MS), gel permeation chromatography (GPC), and NMR. The polymers were directly dissolved

in water or methylcyclohexane to obtain lyotropic liquid crystalline phases. The preparations of the ordered nanocomposites and mesoporous materials are given in refs 19 and 20.

Au@SiO₂ core/shell nanoparticles were synthesized as described elsewhere.²¹ The Au cores have a diameter of 15 nm; the total diameter of the particles is 75 nm as determined from transmission electron microscopy. Crystals of these core/shell nanoparticles were prepared by centrifugation of the core/shell particles in ethanol in a high-speed centrifuge for 3 h. Tetraethoxysilane was added to gel the colloid lattice during centrifugation. Full details of the crystal synthesis are provided elsewhere.²²

2.2. SAXS. Synchrotron SAXS of lyotropic block copolymer phases was performed on the A2 beamline at HASYLAB/DESY, Hamburg (Germany). The beamline is equipped with a two-dimensional CCD detector (MAR Research) and operates at a fixed wavelength of $\lambda = 0.15$ nm. The sample–detector distance was 3.00 m. Our in-house rotating anode device (Seifert, Ahrensburg) consists of a Cu anode, crossed Göbel mirrors, and an image plate detector (Fuji) at a sample–detector distance of 1.005 m. All samples were measured at ambient temperature. The scattering of the solvent (water, methylcyclohexane) was used as the experimental background. Measurements of the Au@SiO₂ core/shell nanoparticles were performed on the SAXS beamline at ChemMatCARS APS, Chicago. The beamline is equipped with a CCD detector (Bruker) and operates at a wavelength of $\lambda = 0.13$ nm with a sample–detector distance of 1.87 m.

3. Scattering Curves of Ordered Particle Systems

For an isotropic two-phase system consisting of polydisperse particles (phase “1”) with scattering length b_1 and volume fraction ϕ_1 in a matrix (phase “2”) of scattering length b_2 and a volume fraction $\phi_2 = 1 - \phi_1$, separated by sharp interfaces, the scattered intensity per unit volume is given by^{14–16,23}

$$I(q) = (b_1 - b_2)^2 \rho_N \langle F^2(q) \rangle + \langle F(q) \rangle^2 [\langle Z(q) \rangle - 1] \quad (1)$$

where $F(q)$ is the scattering amplitude or Fourier transform of the particle form, ρ_N is the number density of the particles, and $Z(q)$ is the lattice factor describing the spatial distribution of the particles. The variable q is the scattering vector given by $q = 4\pi/\lambda \sin(\vartheta/2)$ where λ is the wavelength and ϑ is the scattering angle. The angular brackets $\langle \dots \rangle$ denote an average with respect to the particle size distribution and the spatial distribution of particles,¹³ which are assumed to be independent. This decoupling approximation allows one to factorize the scattering intensity into contributions from the particle form factor and particle structure factor. The decoupling approximation will break down for very polydisperse systems.²⁴ For X-ray, neutron, and light scattering experiments, the scattering lengths b_i have units of [m], which together with the unit of the number density ρ_N (in [m⁻³]) yields for the scattered intensity the usual units of [m⁻¹].

3.1. Particle Form Factor. The particle form factor $P(q)$ for spheres, cylinders, and lamellae or disks with cross-sectional radius R , length L and disk radius $R_D = L$ (Figure 1) is given by

$$P(L, R, q) = F^2(L, R, q) \quad (2)$$

The scattering amplitude $F(L, R, q)$ for long cylindrical and sheet-like particles can be factorized into

$$F(L, R, q) = F_{d\parallel}(L, q) F_{d\perp}(R, q) \quad (3)$$

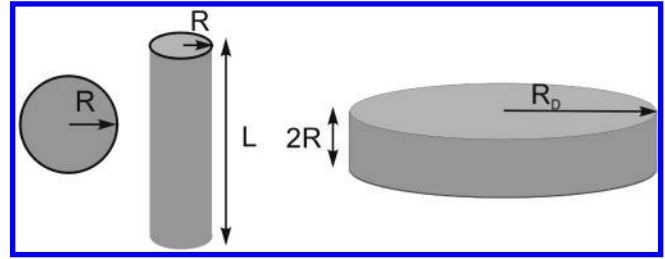


Figure 1. Schematic presentation of different particle shapes, i.e., spheres, cylinders, and disks or lamellae, with radius R , cylinder length L , and disk radius R_D as considered in the text.

where $F_{d\parallel}(L, q)$ is the longitudinal contribution parallel to the cylinder axis or normal to the lamella and $F_{d\perp}(R, q)$ is the contribution from the cross-section of the particle. The variable d is the dimensionality of the particles, i.e., $d = 1$ for lamellae or bilayers, $d = 2$ for cylinders, and $d = 3$ for spheres. Since spheres are isotropic, the factorization may be formally introduced by setting $F_{3\parallel}(L, q) = 1$ (see Table 1). The factorization for cylinders and lamellae is a good approximation for high aspect ratios, i.e., if $L/R_D > 10R$, which is most often the case for lyotropic liquid crystalline phases and mesoscopically ordered materials derived therefrom.

The cross-sectional scattering amplitude $F_{d\perp}(R, q)$ of a d -dimensional homogeneous particle is given by

$$F_{d\perp}(R, q) = {}_0F_1 \left[\frac{d+2}{2}; -\frac{q^2 R^2}{4} \right] \quad (4)$$

where ${}_0F_1[b_1; x]$ is the hypergeometric function whose definition and properties are outlined in the Appendix. For spheres, cylinders, and lamellae it reduces to simpler functions given in Table 1. The square of $F_{d\perp}(R, q)$ is also a hypergeometric function, i.e.

$$F_{d\perp}^2(R, q) = {}_1F_2 \left[\frac{d+1}{2}, \frac{d+2}{2}, d+1; -q^2 R^2 \right] \quad (5)$$

The general expressions in eqs 4 and 5 are convenient for the calculation of the averages $\langle F_{d\perp}(R, q) \rangle$ and $\langle F_{d\perp}^2(R, q) \rangle$. The longitudinal scattering amplitudes $F_{d\parallel}(L, q)$ can be obtained from eqs 4 and 5 by substituting $d \rightarrow 3 - d$, i.e.,

$$F_{d\parallel}(L, q) = {}_0F_1 \left[\frac{5-d}{2}; -\frac{q^2 L^2}{4} \right], d = 1, 2 \quad (6)$$

except in the case of spheres ($d = 3$), where $F_{3\parallel}(q) = 1$. Similarly, the square of the longitudinal scattering amplitudes is given by

$$F_{d\parallel}^2(L, q) = {}_1F_2 \left[\frac{4-d}{2}, \frac{5-d}{2}, 4-d; -q^2 L^2 \right], d = 1, 2 \quad (7)$$

These functions reduce to simpler functions as given in Table 1. The form factors $P(q)$ have the asymptotes

$$\lim_{q \rightarrow \infty} q^4 P(q) = P_{d\infty} \quad (8)$$

where the $P_{d\infty}$ are also given in Table 1 together with the particle volumes V_{dp} .

3.2. Particle Size Distribution. The particle size distribution can be taken into account by averaging the form factor $P(L, R, q)$ over independent size distributions with respect to L and R , yielding

$$\langle P(L, R, q) \rangle = \langle F_{d\parallel}^2(L, q) \rangle \langle F_{d\perp}^2(R, q) \rangle \quad (9)$$

TABLE 1: Dimensionality d , Longitudinal Form Factor $F_{d||}(q)$, Cross-Sectional Form Factor $F_{d\perp}(q)$, Averages $\langle F_{d||}(q) \rangle$, $\langle F_{d\perp}(q) \rangle$, $\langle F_{d||}^2(q) \rangle$, and $\langle F_{d\perp}^2(q) \rangle$ for a Schulz–Zimm Distribution, Orientationally Averaged Longitudinal Part $F_{d||}^2(q)_{or}$, Zeros z_n of the Cross-Sectional Form Factor $F_{d\perp}^2(q)$, High- q Limit of the Form Factor $P(q)$ and Particle Volume V_{dp} for Different Particle Shapes

	lamellae	cylinders	spheres
d	1	2	3
$F_{d }(q)$	$2J_1(qR_D)/(qR_D)$	$\sin(qL/2)/(qL/2)$	1
$F_{d\perp}(q)$	$\sin(qR)/(qR)$	$2J_1(qR)/(qR)$	$(3/(qR)^3)(\sin(qR) - qR\cos(qR))$
$\langle F_{d }(q) \rangle$	${}_2F_1[(z+1)/2, (z+2)/2, 2; -q^2R_D^2]$	$\langle \sin(qL/2)/(qL/2) \rangle$	1
$\langle F_{d\perp}(q) \rangle$	$\langle \sin(qR)/(qR) \rangle$	${}_2F_1[(z+1)/2, (z+2)/2, 2; -q^2R_z^2]$	$3\langle \sin(qR)/(qR)^3 \rangle - \langle \cos(qR)/(qR)^2 \rangle$
$\langle F_{d }^2(q) \rangle$	${}_3F_2[3/2, (z+1)/2, (z+2)/2, 2, 3; -4q^2R_D^2]$	$\langle \sin^2(qL/2)/(qL/2)^2 \rangle$	1
$\langle F_{d\perp}^2(q) \rangle$	$\langle \sin^2(qR)/(qR)^2 \rangle$	${}_3F_2[3/2, (z+1)/2, (z+2)/2, 2, 3; -4q^2R_z^2]$	$9\langle \sin^2(qR)/(qR)^6 \rangle - 2\langle \sin(qR)\cos(qR)/(qR)^5 \rangle + \langle \cos^2(qR)/(qR)^4 \rangle$
$F_{d }^2(q)_{or}$	$(2/(qR_D)^2)(1 - J_1(2qR_D)/(qR_D))$	$(2/(qL))\text{Si}(qL) - (\sin(qL/2)/(qL/2))^2$	1
z_n	$qR = n\pi$ $z_n/z_1 = 1, 2, 3, 4, 5, \dots$	$qR = n\pi + \zeta$, $\zeta \approx 0.69467\dots$ $z_n/z_1 = 1, 1.83, 2.65, 3.48, 4.30$	$qR = n\pi + \pi/2$ $z_n/z_1 = 1, 1.71, 2.42, 3.12, 3.83, \dots$
$P_{d\infty}$	$1/(R_D^2R^2)$	$4/(LR^3)$	$9/(2R^4)$
V_{dp}	$2\pi R_D^2R$	πR^2L	$4\pi/(3R^3)$

In most cases, the Schulz–Zimm distribution is used, which for a function $f(X, q)$ with $X = L, R_D, R$ yields

$$\langle f(\bar{X}, q) \rangle = \int_0^\infty f(X, q) h(X) dX \quad (10)$$

with

$$h(X) = \frac{(z+1)^{z+1} X^z}{\bar{X}^{z+1} \Gamma(z+1)} \exp\left[-(z+1) \frac{X}{\bar{X}}\right] \quad (11)$$

with the average \bar{X} and the relative standard deviation $\sigma_X = (z+1)^{-1/2}$. The distribution is normalized such that $\int_0^\infty h(X) dX = 1$. The averages for the particle cross-sectional scattering amplitudes for a given dimensionality d are

$$\langle F_{d\perp}(q) \rangle = \int_0^\infty {}_0F_1\left[\frac{d+2}{2}; -\frac{q^2 R^2}{4}\right] h(R) dR = {}_2F_1\left[\frac{z+1}{2}, \frac{z+2}{2}, \frac{d+2}{2}; -q^2 R_z^2\right] \quad (12)$$

$$\langle F_{d\perp}^2(q) \rangle = \int_0^\infty {}_1F_2\left[\frac{d+1}{2}, \frac{d+2}{2}, \frac{d+2}{2}; -q^2 R^2\right] h(R) dR = {}_3F_2\left[\frac{d+1}{2}, \frac{z+1}{2}, \frac{z+2}{2}, \frac{d+2}{2}, d+1; -4q^2 R_z^2\right] \quad (13)$$

with $R_z = \bar{R}/(z+1)$. The derivation is given in the Appendix. In the case $d = 1, 3$ (lamellae, spheres), these expressions reduce to simpler expressions as given in Table 1 and in the Appendix. In the case of $d = 2$ (cylinders), there are no simpler analytical expressions.

The averages for the longitudinal scattering amplitudes for dimensionalities $d = 1, 2$ can again be obtained by substituting $d \rightarrow 3 - d$, i.e.,

$$\langle F_{d||}(q) \rangle = \int_0^\infty {}_0F_1\left[\frac{5-d}{2}; -\frac{q^2 L^2}{4}\right] h(L) dL = {}_2F_1\left[\frac{z+1}{2}, \frac{z+2}{2}, \frac{5-d}{2}; -q^2 \bar{L}^2\right], d = 1, 2 \quad (14)$$

$$\langle F_{d||}^2(q) \rangle = \int_0^\infty {}_1F_2\left[\frac{4-d}{2}, \frac{5-d}{2}, \frac{5-d}{2}; -q^2 L^2\right] h(L) dL = {}_3F_2\left[\frac{4-d}{2}, \frac{z+1}{2}, \frac{z+2}{2}, \frac{5-d}{2}, 4-d; -4q^2 \bar{L}^2\right], d = 1, 2 \quad (15)$$

with $L_z = \bar{L}/(z+1)$. In the case of spheres ($d = 3$), the longitudinal scattering amplitudes are equal to unity. The expressions for spheres, cylinders, and lamellae are summarized in Table 1.

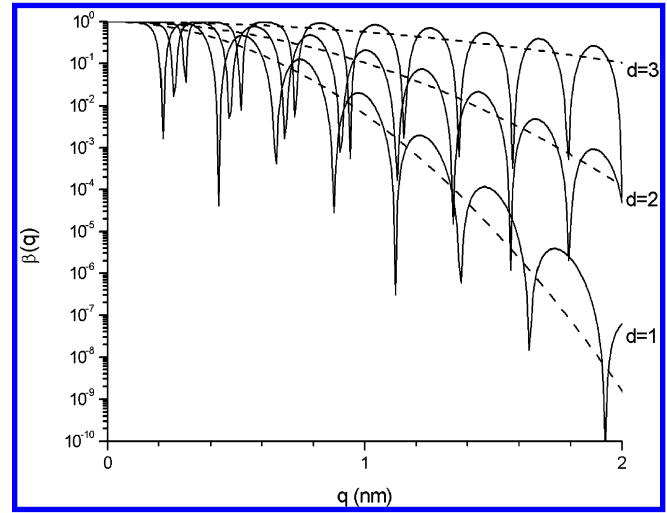


Figure 2. Ratio $\beta(q)$ (eq 16) for spheres ($d = 3$, $\sigma_R = 0.05$), cylinders ($d = 2$, $\sigma_R = 0.10$), and disks ($d = 1$, $\sigma_R = 0.15$) with a radius $R = 15$ nm. The dashed lines are the Gaussian approximations for the nonoscillating decay (eq 17).

Whereas the polydispersity in particle diameter R has a pronounced influence on the scattering curves in the range of scattering vectors $q > 2\pi/a$, where a is the lattice spacing, polydispersities for large cylinder lengths L or disk radii R_D have little influence. Throughout the following calculations we approximate $\langle F_{d||}(L, q) \rangle = F_{d||}(L, q)$ and $\langle F_{d\perp}^2(L, q) \rangle = F_{d\perp}^2(L, q)$ and use only the orientationally averaged longitudinal part $F_{d||}^2(L, q)_{or}$ as given in Table 1.

For the calculation of the scattered intensity in eq 1, the ratio

$$\beta(q) = \frac{\langle F_d(q) \rangle^2}{\langle F_d^2(q) \rangle} = \frac{\langle F_{d\perp}(R, q) \rangle^2}{\langle F_{d\perp}^2(R, q) \rangle} \quad (16)$$

is needed. The case for $d = 3$ has been previously derived in ref 23. The effect of this ratio on the scattered intensity can be inferred from the asymptotic expansion of the hypergeometric functions for large z (small σ_R).²⁵ The expansion consists of an oscillating part and a nonoscillating part, $e^{-(z+1)q^2 R_z^2}$, which yields as an approximation for the nonoscillating contribution

$$\beta(q) \approx e^{-\sigma_R^2 R^2 q^2} \quad (17)$$

Figure 2 compares $\beta(q)$ (eq 16) with the Gaussian approximation of the nonoscillating part in eq 17. It describes the

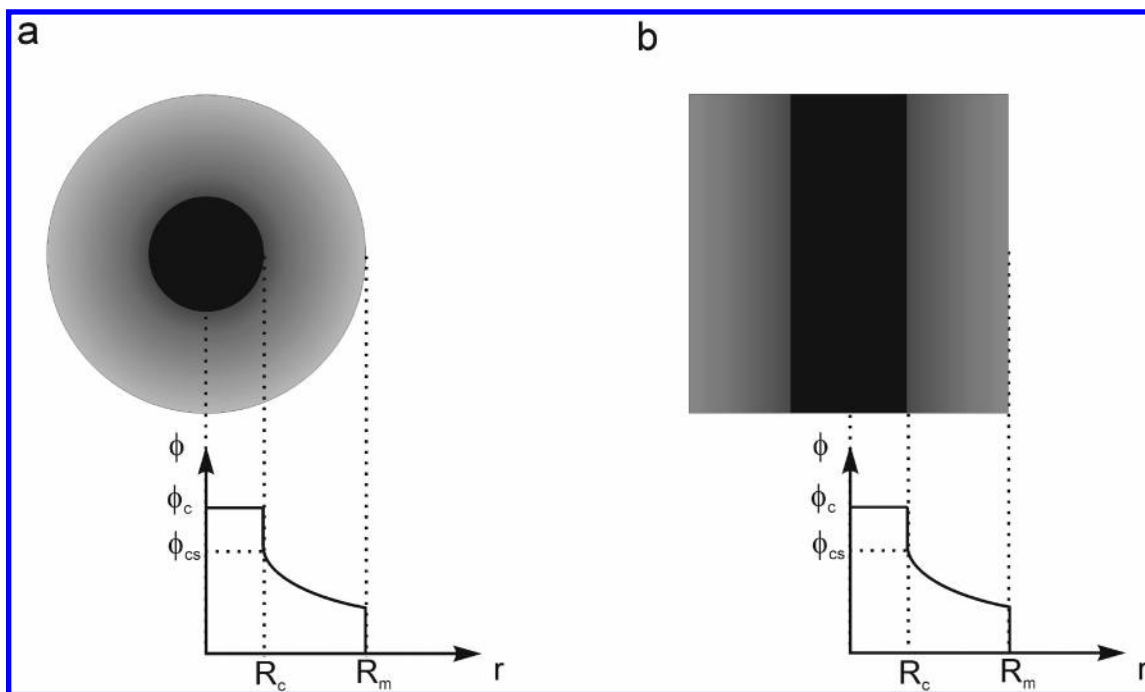


Figure 3. Schematic presentation of core/shell particles with core radius R_c , overall radius R_m , core density ρ_c and shell density ρ_s . The shell density profile decays as $r^{-\alpha}$.

nonoscillating decay of the ratio $\beta(q)$ for different particle dimensionalities and low polydispersities ($\sigma_R < 0.3$). The expression is similar to the Debye–Waller factor $e^{\sigma_a^2 \bar{a}^2 q^2}$ introduced below for the lattice point correlations and similarly results in a decay of the Bragg intensities with increasing q .

3.3. Core/Shell Particles. In many cases, colloidal particles have a core/shell structure as schematically shown in Figure 3. Examples are surfactant, lipid and block copolymer micelles with hydrophobic cores and hydrophilic headgroups or polymer layers, or core/shell nanoparticles. Similarly, particles in ordered nanocomposites or pores in mesoporous materials may be coated by a layer of a different material and therefore can be considered to have a core/shell structure. The structure of the outer layer can in many cases be described by an algebraic density profile of the form $\phi(r) = r^{-\alpha}$.¹⁷ For a homogeneous layer we have $\alpha = 0$, whereas for dense d -dimensional polymer layers or brushes theories predict $\alpha = 2(d - 1)/3$,²⁶ i.e., $\phi(r) = r^0$ for planar brushes or homogeneous domains, $\phi(r) = r^{-2/3}$ for cylindrical brushes, and $\phi(r) = r^{-3/4}$ for spherical brushes. This type of $r^{-\alpha}$ scaling has been experimentally verified for spherical block copolymer micelles.²⁷

The density profile for a lamellar, cylindrical, or spherical core/shell particles with a homogeneous core and an $r^{-\alpha}$ density profile (Figure 3) can be written as

$$\phi(r) = \begin{cases} \phi_c, & \text{for } 0 \leq r < R_1 = R_c \quad (\text{core}) \\ \phi_s = \phi_{cs} \left(\frac{r}{R_c} \right)^{-\alpha}, & \text{for } R_c \leq r < R_2 = R_m \quad (\text{shell}) \\ 0, & \text{for } R_m \leq r \end{cases} \quad (18)$$

where ϕ_c is the volume fraction of the core, ϕ_{cs} is the volume fraction of the shell at the core/shell interface, $\phi_s(r)$ is the volume fraction of the shell, R_c the core radius, and R_m the total radius of the core/shell particle. The scattering length of the core and the shell are given by $b_{1c} = (b_{1c}^0 - b_2)\phi_c$ and $b_{1s} = (b_{1s}^0 - b_2)\phi_s$, where b_{1c}^0 is the scattering length of the core material

and b_{1s}^0 is the scattering length of the shell material, respectively. Since the scattering lengths b_{1c}^0 and b_{1s}^0 can be smaller as the scattering length of the solvent b_2 , the scattering lengths of the core and shell b_{1c} and b_{1s} can be negative. This is frequently the case in X-ray scattering of amphiphilic systems, where the hydrophobic core has a smaller electron density compared to water as the solvent.

The scattering amplitude corresponding to eq 18 is given by¹⁷

$$F_{d\perp}(q) = \frac{\left[\frac{1}{d} F_d(0, R_c, q) - \frac{\rho}{(d - \alpha)} F_d(\alpha, R_c, q) + \frac{\rho p^{\alpha-d}}{(d - \alpha)} F_d(\alpha, R_m, q) \right]}{\left[\frac{1}{d} - \frac{\rho}{(d - \alpha)} + \frac{\rho p^{\alpha-d}}{(d - \alpha)} \right]} \quad (19)$$

where

$$F_d(\alpha, R, q) = {}_1F_2 \left[\frac{d - \alpha}{2}, \frac{d + 2 - \alpha}{2}, -\frac{q^2 R^2}{4} \right] \quad (20)$$

and $\rho = [(b_{1s}^0 - b_2)\phi_{cs}]/[(b_{1c}^0 - b_2)\phi_c]$ and $p = R_c/R_m$. For homogeneous shells of constant density ($\alpha = 0$), eq 20 reduces to

$$F_{d\perp}(q) = \left[(1 - \rho) {}_0F_1 \left[\frac{(d + 2)}{2}, -\frac{q^2 R_c^2}{4} \right] + \rho p^{-d} {}_0F_1 \left[\frac{(d + 2)}{2}, -\frac{q^2 R_m^2}{4} \right] \right] / [1 - \rho(1 - p^{-d})] \quad (21)$$

for which the respective expressions ${}_0F_1[x]$ for spheres, cylinders, and lamellae have been compiled in Table 1. For homogeneous particles ($p = 1$ or $\rho = 1$), eq 21 reduces further to $F_{d\perp}(R_m, q)$, and for $\rho = 0$ to $F_{d\perp}(R_c, q)$ given in eq 4.

TABLE 2: Symmetry Factors f_{hkl} for Different Lattice Types

lattice	allowed reflections
LAM	$f_{hkl} = 1$ for all reflections
HEX ($P/6mm$)	$f_{hkl} = 1$ for all reflections
SQ ($P/4mm$)	$f_{hkl} = 1$ for all reflections
SC ($Pm3m$)	$f_{hkl} = 1$ for all reflections
BCC ($Im3m$)	$f_{hkl} = 2$ for $h + k + l = \text{even}$
FCC ($Fm3m$)	$f_{hkl} = 4$ for $(h \wedge k \wedge l) \text{ even}$
	$f_{hkl} = 4$ for $(h \wedge k \wedge l) \text{ odd}$
HCP ($P6/mmc$)	$f_{hkl} = 2$ for $(h + 2k = 3n)$ with l even
	$f_{hkl} = \sqrt{3}$ for $(h + 2k = 3n + 1) \vee (h + 2k = 3n + 2)$ with l odd
	$f_{hkl} = 1$ for $(h + 2k = 3n + 1) \vee (h + 2k = 3n + 2)$ with l even

TABLE 3: Number of Particles per Unit Cell n , Volume of the Unit Cell V_d , Projected d -Dimensional Volume v_d (eq 23), Particle Volume Fraction $\phi = V_{dp}/V_d$, Maximum Volume Fraction ϕ_{\max} , Peak Multiplicities m_{hkl} , Solid Angle Ω_d (eq 23), and Nearest Neighbor Distance \bar{a} for Different Lattice Types

	lam	hex ($P6/mmm$)	sq ($P4/mm$)	bcc ($Im3m$)	fcc ($Fm3m$)	hcp ($P6/mmc$)	sc ($Pm3m$)
n	1	1	1	2	4	2	1
V_d	$\pi R_d^2 a$	$\sqrt{3}a^2 L/2$	$a^2 L$	a^3	a^3	$\sqrt{2}a^3$	a^3
v_d	a	$\sqrt{3}a^2/2$	a^2	a^3	a^3	$\sqrt{2}a^3$	a^3
ϕ	$2R/a$	$2\pi R^2/(\sqrt{3}a^2)$	$\pi R^2/a^2$	$8\pi R^3/(3a^3)$	$16\pi R^3/(3a^3)$	$8\pi R^3/(3\sqrt{2}a^3)$	$4\pi R^3/(3a^3)$
ϕ	1	$\pi/(2\sqrt{3}) \approx 0.907$	$\pi/4 \approx 0.785$	$\pi\sqrt{3}/8 \approx 0.680$	$\pi\sqrt{2}/6 \approx 0.740$	$\pi/(3\sqrt{2}) \approx 0.740$	$\pi/6 \approx 0.524$
m_{hkl}	$m_h = 1$	$m_{h0} = 6$ $m_{hh} = 6$ $m_{hk} = 12$	$m_{h0} = 4$ $m_{hh} = 4$ $m_{hk} = 8$	$m_{h00} = 6$ $m_{hh0} = 12$ $m_{hhh} = 8$ $m_{hkk} = 24$ $m_{hkh} = 24$ $m_{hkl} = 48$	$m_{h00} = 6$ $m_{hh0} = 12$ $m_{hhh} = 8$ $m_{hkk} = 24$ $m_{hkh} = 24$ $m_{hkl} = 48$	$m_{h00} = 6$ $m_{h0l} = 2$ $m_{hh0} = 6$ $m_{hkl} = 12$ $m_{hkl} = 12$ $m_{hkl} = 24$	$m_{h00} = 6$ $m_{hh0} = 12$ $m_{hhh} = 8$ $m_{hkk} = 24$ $m_{hkh} = 24$ $m_{hkl} = 48$
Ω_d	1	2π	2π	4π	4π	4π	4π
\bar{a}	a	a	a	$\sqrt{3}a/2$	$\sqrt{2}a/2$	a	a

For the calculations of $\langle F_{d\perp}(q) \rangle$ for general α , the average is equal to

$$\begin{aligned} \langle F_d(\alpha, R, q) \rangle &= \int_0^\infty {}_1F_2 \left[\frac{d-\alpha}{2}, \frac{d+2-\alpha}{2}; -\frac{q^2 R^2}{4} \right] h(R) dR \\ &= {}_3F_2 \left[\frac{d-\alpha}{2}, \frac{z+1}{2}, \frac{z+2}{2}; \frac{d+2-\alpha}{2}, -\frac{q^2 R^2}{2} \right] \end{aligned} \quad (22)$$

The asymptotic expansions at large q for the calculation of the averages $\langle F_{d\perp}(q) \rangle^2$ and $\langle F_{d\perp}(q) \rangle$ are given in the Appendix. Generally, the asymptotes of the form factors of core/shell structures exhibit no simple Porod laws as in eq 8.

3.4. Lattice Factor. Using the Miller indices (hkl) for a given crystal lattice plane, the lattice factor for an ideal undistorted lattice, $Z_0(q)$, can be written according to Ruland and Wolff^{15,16} as

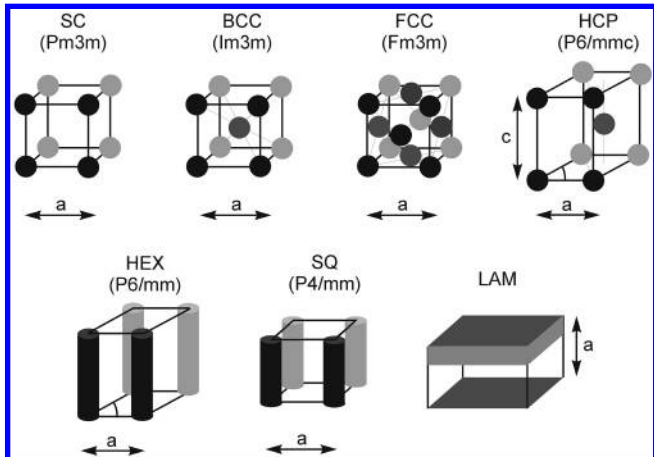
$$Z_0(q) = \frac{(2\pi)^{d-1} c}{n v_d \Omega_d q^{d-1}} \sum_{\{hkl\}} m_{hkl} f_{hkl}^2 L_{hkl}(q) \quad (23)$$

where n is the number of particles per unit cell, f_{hkl} is the symmetry factor that takes into account symmetry-related extinction rules (Table 2), v_d is the volume ($d = 3$), surface ($d = 2$), or long-period ($d = 1$) of the d -dimensional unit cell, Ω_d is the d -dimensional solid angle, and $L_{hkl}(q)$ is a normalized peak shape function. The summation is over all sets of reflections $\{hkl\}$ where m_{hkl} is the corresponding peak multiplicity which, e.g., for a cubic phase in case of $\{h\bar{h}0\}$ is $m_{h\bar{h}0} = 12$ (corresponding to the reflections $(h\bar{h}0, h\bar{h}0, h\bar{h}0, h\bar{h}0, h\bar{h}0, h\bar{h}0, h\bar{h}0, h\bar{h}0, h\bar{h}0, h\bar{h}0, h\bar{h}0, h\bar{h}0)$). The term c is a constant of order unity whose exact value is calculated using the Porod invariant as outlined below. The values of these parameters for different crystal lattices (lam, sq, hex, sc, bcc, fcc, hcp) are given in Table 3 together with the volume of the unit cell, V_d . The

TABLE 4: Positions of the Reflections q_{hkl} for Different Lattice Types

lamellae ($d=1$)	$q_h = 2\pi h/a$
hexagonal ($d=2$)	$q_{hk} = 4\pi\sqrt{h^2 + hk + k^2}/(\sqrt{3}a)$
square ($d=2$)	$q_{hk} = 2\pi\sqrt{h^2 + k^2}/a$
cubic ($d=3$)	$q_{hkl} = 2\pi\sqrt{h^2 + k^2 + l^2}/a$
hexagonal ($d=3$)	$q_{hkl} = 2\pi\sqrt{4/3(h^2 + hk + k^2) + 3l^2}/a$

term a is the unit cell dimension and \bar{a} is the closest distance between next neighbors. The volume fraction is given by $\phi = V_{dp}/V_d$; the maximum volume fraction ϕ_{\max} is obtained for $R = \bar{a}/2$. For hcp, the relation between the two unit cell dimensions of the hexagonal Bravais lattice is $c = \sqrt{8/3}a$. The peak positions q_{hkl} are given in Table 4. The crystal structures are depicted in Figure 4.

**Figure 4.** Schematic presentation of different lattices with unit cell dimension a and c as considered in the text. SC = simple cubic, BCC = body centered cubic, FCC = face centered cubic, HCP = hexagonally close packing, HEX = 2D-hexagonal packing, SQ = 2D-square packing, LAM = 1D-packing.

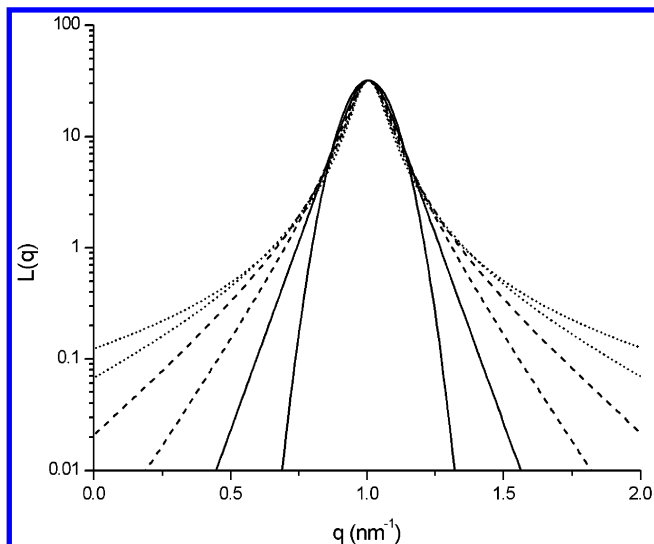


Figure 5. Peak shapes $L(q)$ (eq 27) for different values of the peak shape parameter of $\nu = 0.001$ (gray dotted), 0.1 (black dotted), 0.2 (gray dashed), 0.4 (black dashed), 1 (gray solid) and 1000 (black solid) showing the evolution of the peak shape from Lorentzian to Gaussian.

3.5. Lattice Disorder. For lattices with translational disorder where the displacements from the ideal lattice points are statistically independent (static disorder of the first kind), one can assume a Gaussian lattice point distribution with zero mean and a relative mean square displacement σ_a^2 . In this case the lattice factor is given by²⁸

$$Z(q) = Z_0(q)G(q) + (1 - G(q)) \quad (24)$$

where the first term, $Z_0(q)G(q)$, describes the decay of the intensity of the Bragg peaks, whereas the second term, $1 - G(q)$, describes the concomitant increase of the diffuse scattering. $G(q)$ is given by

$$G(q) = \exp[-\sigma_a^2 \bar{a}^2 q^2] \quad (25)$$

which is known as the Debye–Waller factor for thermal disorder. Here, \bar{a} is the next nearest neighbor distance between adjacent particles, which for different lattice types is given in Table 3. In the case of lamellar or bilayer systems, the relative displacement is related to the Caillé parameter η ^{12,29} as

$$\eta = 8\sigma_a^2 \quad (26)$$

which characterizes thermal displacement fluctuations in lipid bilayers. If the interlamellar forces are dominated by entropic undulations, the Caillé parameter has a value of $\eta = 4/3(1 - 2R/a)^2$, where $2R$ is the bilayer thickness.³⁰ σ_a in eq 26 is comparable to the Hosemann g -factor, which describes the relative standard deviation of the mean distance between particles in paracrystal theory (static disorder of the second kind).

3.6. Peak Shape. $L_{hkl}(q)$ is a normalized peak shape function for which Lorentzian, Gaussian, pseudo-Voigt, or Pearson functions are commonly used.³¹ A general and versatile normalized peak shape function is adopted from a function given by Burger and Micha³² with

$$L_{hkl}(q) = \frac{2}{\pi\delta} \prod_{n=0}^{\infty} \left(1 + \frac{\gamma_n^2}{(n + \nu/2)^2 \pi^2 \delta^2} \right)^{-1} \quad (27)$$

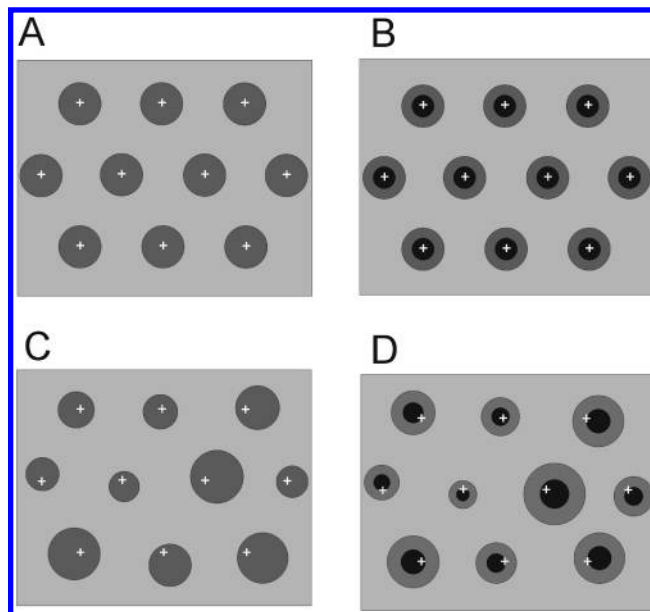


Figure 6. Schematic presentation of ideal lattices of monodisperse homogeneous (A) and core/shell particles (B), as well as distorted lattices of polydisperse homogeneous (C) and core/shell particles (D). Cases (C) and (D) are typical for ordered mesoscopic structures and are described by eq 30.

where $x = (q - q_{hkl})$ and

$$\gamma_\nu = \pi^{1/2} \frac{\Gamma[(\nu + 1)/2]}{\Gamma[\nu/2]}$$

The peak shape is normalized such that $\int_{-\infty}^{\infty} L_{hkl}(q) dq = 1$. Here, q_{hkl} is the peak position and δ the peak width which can be related to the domain size D of the ordered domain via the Debye–Scherrer equation $D = 2\pi/\delta$. This peak shape function is convenient since by adjusting the parameter ν the peak shape can be continuously varied between a Lorentzian ($\nu \rightarrow 0$) and a Gaussian ($\nu \rightarrow \infty$), i.e.,

$$L_{hkl}(x) = \begin{cases} \frac{\delta/2\pi}{x^2 + (\delta/2)^2} & \text{for } \nu \rightarrow 0 \text{ (Lorentzian)} \\ \frac{2}{\pi\delta} \exp\left[-\frac{4x^2}{\pi\delta^2}\right] & \text{for } \nu \rightarrow \infty \text{ (Gaussian)} \end{cases} \quad (28)$$

where, in case of the Lorentzian, δ is equal to the full width at half-maximum (fwhm), whereas in case of a Gaussian δ is related to the standard deviation as $\sigma = \sqrt{\pi/8}\delta$. Inserting eq 24 into eq 1 yields for the scattered intensity

$$I(q) = (b_1 - b_2)^2 \rho_N P(q) [1 + \beta(q)(Z_0(q) - 1)G(q)] \quad (29)$$

which can be rewritten as

$$I(q) = (b_1 - b_2)^2 \rho_N P(q) S(q) \quad (30)$$

where $S(q)$ is the structure factor. This approach considers the effect of the particles (via their first and second moment of the particle size distribution) and of the lattice (via the first and second moment of the distribution of lattice points) on the scattered intensity $I(q)$. The particle size and lattice point distribution is schematically depicted in Figure 6. According to eqs 17 and 25, both effects lead to damping of the higher

order Bragg reflections by a factor $e^{-(\sigma_a^2 a^2 + \sigma_R^2 R^2)q^2}$, with additional suppression of Bragg reflections at the zeroes of $\beta(q)$. The additivity of both contributions in the argument of the exponential decay results from the assumption of their statistical independence.

It is straightforward to consider also other polymer or colloid structures with their respective form factors $P(q)$ and structure factors $Z_0(q)$ which, e.g., are well compiled in a review by Pedersen.³³

3.7. Grazing Incidence Scattering (GISAXS). Eq 30 also allows one to describe the 2-dimensional in-plane order of mesoscopically structured thin films or monolayers. The in-plane order can be derived from the diffuse scattering intensity of grazing incidence small-angle X-ray (GISAXS) or neutron scattering (GISANS) patterns.³⁴ The total detected intensity is given by the sum of the specularly reflected intensity, the intensity scattered due to the surface roughness, and the diffuse scattering, which is related to the density fluctuations in the bulk of the thin film. The diffuse scattering is given by³⁵

$$I_d(q) = \frac{k_c C}{(4\pi r^2)} |T_i|^2 |T_f|^2 I_{\text{diff}}(q) \quad (31)$$

where k_c is the vertical component of the momentum vector at the critical angle of total external reflection, C the illuminated area, T the Fresnel transmission coefficients of the incident and reflected waves, and $I_{\text{diff}}(q)$ is the “diffuse structure factor”. With the film positioned in the xy -plane, the diffuse scattering has components along q_{xy} (“out of plane of incidence”) and q_z normal to the xy -plane. The scattering amplitude of cylindrical particles with their long axis normal to the xy -plane is then given by the cross-sectional contribution $F_{2\perp}(q_{xy}R)$ and the longitudinal part $F_{2\parallel}(q_z L)$. The diffuse part of the scattering intensity is then given by $I_{\text{diff}}(q) = I_N(q)$ where the form factor $P(q)$ in eq 30 is given by

$$P_2(q_{xy}, q_z) = \langle F_{2\perp}^2(q_{xy}R) \rangle \langle F_{2\parallel}^2(q_z L) \rangle \quad (32)$$

Thereby, the in-plane order of thin films as measured by grazing incidence out-of-plane scans can be described for hexagonal or square arrangements of cylindrical domains having a homogeneous or core/shell structure. Because of the particular orientation of the cylinders (the long axis being in z -direction, the cross-section in the xy -plane) the factorization in eq 3 is valid for any axial ratio of the cylinder, in particular also for disks, where $L \ll R$. The in-plane form factor has an asymptote of $\lim_{q \rightarrow \infty} \langle F_{2\perp}^2(qR) \rangle = 4/\pi(qR)^{-3}$, so that a characteristic q^{-3} scaling is expected for out-of-plane scans of domains with spherical cross-sections.

In the case of spherical particles, the form factor contribution to the diffuse scattering is isotropic and given by

$$P_3(q_{xy}, q_z) = \langle F_{3\perp}^2(qR) \rangle \quad (33)$$

where $q = \sqrt{q_{xy}^2 + q_z^2}$, in agreement with ref 35.

Thus, the description of ordered domains using eq 30 is applicable not only to the scattering of bulk mesoscopic materials but also to the in-plane scattering of thin films or monolayers. Such structures are of considerable relevance for the structuring of surfaces by lithography or self-assembly for catalysis, sensing, and electrooptical applications. It is straightforward to extend the description to multilayers by considering the respective reflections of the structure factor $S(q_{xy}, q_z)$. By further consideration of the Fresnel transmission functions $T(q_z)$ -

of the thin film, the complete GISAXS or GISANS pattern can be calculated.

3.8. Integral Scattered Intensity. For two-phase systems, the factor c in eq 23 ensures that the integral scattered intensity as characterized by the Porod invariant Q is given by

$$Q = \int_0^\infty I(q) q^2 dq = 2\pi^2 \phi(1 - \phi) \frac{(b_1 - b_2)^2}{V_{pd}^2} \quad (34)$$

which is the total scattering length of the sample. Porod's invariant is related to the asymptotic behavior of the scattered intensity at high q , i.e.,

$$Q = \frac{\pi}{4} l_p (b_1 - b_2)^2 \rho_N \lim_{q \rightarrow \infty} q^4 P(q) S(q) \quad (35)$$

where l_p is the Porod length or chord length which is related to the surface per unit volume as

$$l_p = \frac{4\phi(1 - \phi)}{S_V} \quad (36)$$

This relation is rigorous for any microphase-separated system as long as the interface is sharp. For some materials, e.g., polymeric systems, interfaces can be relatively diffuse, so that this relation may not be applicable. As outlined above, core/shell particles do not in general have a simple Porod behavior, so that the following arguments apply only for homogeneous two-phase systems.

In the case of homogeneous two-phase systems with sharp interfaces with a given dimensionality d , the surface per unit volume is given by

$$S_V = \frac{d\phi}{R} \quad (37)$$

from which the specific surface area A_{sp} (in m^2/g) for a mesoporous material with wall- or matrix density ρ_{sp} can be calculated as

$$A_{sp} = \frac{S_V}{(1 - \phi)\rho_{sp}} \quad (38)$$

For $q \rightarrow \infty$, the Debye–Waller factor approaches $G(q) \rightarrow 0$, so that $S(q) \rightarrow 1$, and the corresponding limit for the scattered intensity is given by $\lim_{q \rightarrow \infty} I(q) = P_{d\infty} q^{-4}$, with $P_{d\infty}$ given in Table 1. Combining eqs 34–37 and inserting for the particle density $\rho_N = n/V_d$, i.e., the number of particles per unit cell, we obtain a closure relation

$$\frac{\pi R n}{d V_d} (1 - \phi)(b_1 - b_2)^2 P_{d\infty} = \int_0^\infty I_N(q) q^2 dq \quad (39)$$

which determines the coefficient c of the lattice factor $Z_0(q)$ in eq 23. In the examples considered below, deviations from $c = 1$ are only up to a few percent.

3.9. Limiting Behavior for $q \rightarrow 0$. In the thermodynamic limit $q \rightarrow 0$, the scattering intensity is related to the fluctuation in particle number density $\delta\rho_N$ or the isothermal osmotic compressibility χ_T as

$$\lim_{q \rightarrow 0} \tilde{I}(q) = \langle \delta\rho_N^2 \rangle = kT \chi_T \rho_N \quad (40)$$

where $\tilde{I}(q) = I(q) (\rho_1 - \rho_2)^{-2} \rho_N^{-1}$ and kT is the thermal energy. In the limit $q \rightarrow 0$ the form factor $P(q)$ (eq 2), the fluctuation

term $\beta(q)$ (eq 16), and the Debye–Waller factor $G(q)$ (eq 30) all approach unity. Due to the q^{1-d} singularity of the lattice factor $Z_0(q)$ (eq 23), the scattering intensity $\tilde{I}(0)$ will diverge for the case of cylinders ($d = 2$) and spheres ($d = 3$), but not for lamellae ($d = 1$). This parallels the behavior of the structure factor in paracrystal theory, where intensity upturns for $q \rightarrow 0$ have been reported for spheres (three-dimensional paracrystal) but not for lamellae (one-dimensional paracrystal).⁹ In paracrystal theory, the upturn of a scattering curve at $q \rightarrow 0$ corresponds to the contribution of the zero-order scattering related to the finite size of the paracrystal. For the one-dimensional paracrystal, as q approaches zero, the intensity $Z(q)$ continuously decreases to the limiting value of σ_a^2 and the intensity upturn is not found. For the three-dimensional paracrystal there is an intensity upturn to a value of $\sigma_{a,\text{eff}}^2$, which goes to infinity for a random orientation of paracrystals with spherically symmetric distortions of the lattice points.⁹ In eq 23, the q^{1-d} singularity similarly occurs as a consequence of assuming a random orientation of the lattice, so that the angular average of the lattice factor in reciprocal space yields a factor of $(2\pi q)^{-1}$ in the two-dimensional, and a factor of $(4\pi q^2)^{-1}$ in the three-dimensional case. In eq 23, the zero-order peak is not explicitly considered because of the q^{1-d} singularity and because its intensity depends also on the scattering length difference between the lattice inside and outside, which is a priori not known.

Due to the singularity and since structural features on length scales $d > a$, such as packing defects, grain boundaries or fluctuations decaying on larger length scales are only indirectly considered via the domain size D , eq 30 is not expected to give good agreement with experimentally determined scattering curves in the range of scattering vectors $q < 2\pi/a$. However, for $q \geq 2\pi/a$, this approach describes remarkably well experimentally measured high-resolution scattering curves of mesoscopically ordered materials as will be shown and discussed below. The use of factorizations (eq 3) and quickly converging series expansions (eqs 4–7) facilitate computing and allow efficient implementation into fitting routines. It allows one to quickly extract the set of parameters $\{a, \sigma_a, R, \sigma_R, D, \nu\}$ from measured scattering curves involving spheres, cylinders, and bilayers or lamellae. In addition, the parameters $\{R_m, \alpha, \rho\}$ can be derived for core/shell systems. Parameters such as the cylinder length L or the disk radius R_D are difficult to determine because for nearly all mesoscopically ordered materials $L, R_D \gg a$. All curves are fitted using a Levenberg–Marquardt algorithm which quickly converges and allows one to obtain the relative error of the fit parameters. An executable trial version of the program can be obtained from the author (<http://www.chemie.uni-hamburg.de/pc/sfoerster/software.html>). The analysis allows also to take into account the contribution of the background scattering as

$$\tilde{I}(q) = I_{\text{sample}} - kI_{\text{solvent}} \quad (41)$$

where the constant k is the ratio of the transmission of sample and solvent, assuming measuring times and primary beam intensity to be equal. If the constant k is unknown, it can be treated as an adjustable parameter. If no solvent or background data are available, a flat q -independent background can be subtracted. Geometrical resolution effects are not taken into account and are out of the scope of the present paper. They could be incorporated by convoluting the calculated scattering curve with the beam profile as outlined ref 33.

We find that the fits to experimentally measured scattering curves are well comparable to approaches based on paracrystal theory in the case of cubic micellar structures, or based on the

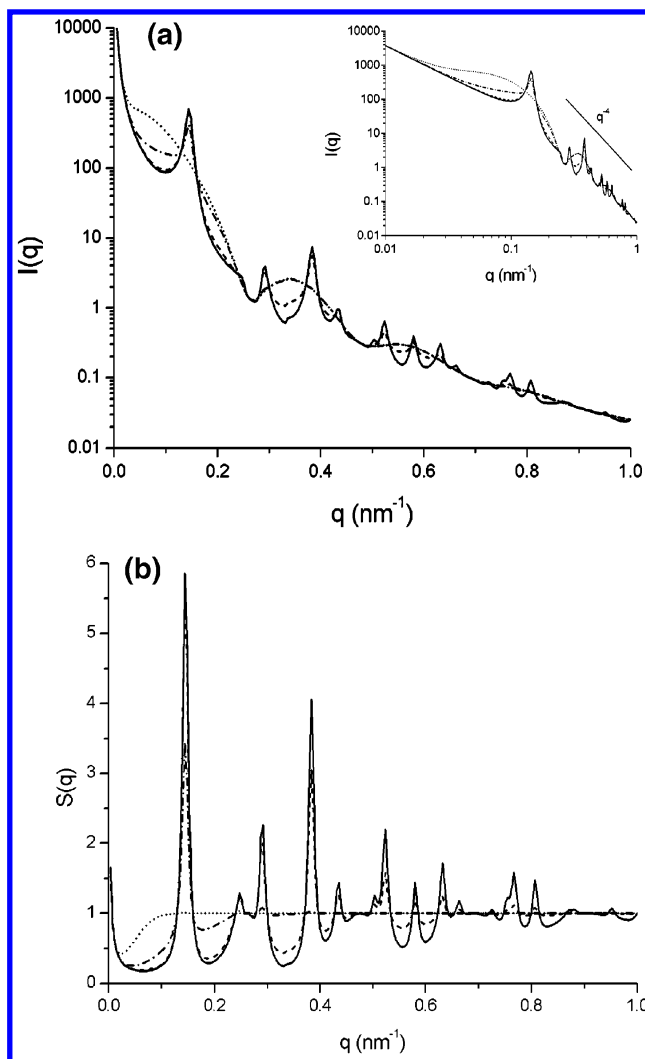


Figure 7. Calculated scattering curves $I(q)$ (a) and structure factor $S(q)$ (b) for a hexagonal lattice of cylinders with $a = 50$ nm, $L = 500$ nm, $R = 15$ nm, $\sigma_R = 0.1$, $D = 500$ nm, and mean displacements of $\sigma_a a = 1$ (solid), 3 (dashed), 10 (dash-dotted), and 30 (dotted) nm with Lorentzian line shapes showing the suppression of higher order peaks with increasing displacement. The inset in (a) shows the characteristic q^{-4} envelope in the high- q regime (Porod law).

Caillé approximations in case of lamellar structures, and allow to nearly quantitatively describe high-resolution synchrotron SAXS and SANS data of many different mesoscopically ordered materials.

4. Results and Discussion

4.1. Structure and Form Factor. The influence of both structure factor $S(q)$ and form factor $P(q)$ on the scattered intensity $I(q)$ can be observed in Figure 7, where the scattered intensity $I(q)$ for hexagonally packed cylinders for different values of the Debye–Waller factor are calculated. The form factor of the cylinders leads to a q^{-4} decay of the scattered intensity (Porod law, see inset in Figure 7a), which considerably weakens the scattered intensity in the high- q region. In the Porod regime, the form factor exhibits damped oscillations, whose positions, periodicity and amplitudes are characteristic for the particle size, shape, and polydispersity. Generally, the relative distances between minima increase in the order sphere \rightarrow cylinder \rightarrow lamellae (see Table 1). Higher order oscillations are damped due to particle polydispersity.

The structure factor $S(q)$ (Figure 7b) exhibits peaks that correspond to reflections characteristic for the symmetry and

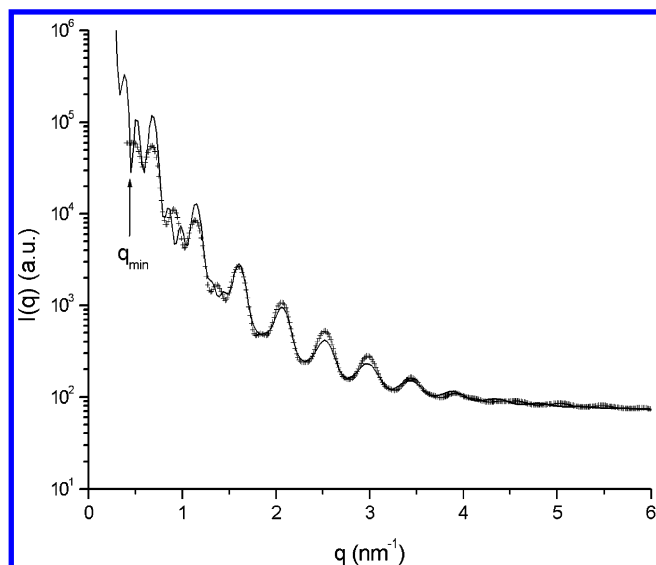


Figure 8. Synchrotron SAXS curve of Au@SiO₂ core/shell particles that have assembled into core/shell superlayers. There is a set of eight major oscillations due to scattering of the core layer with smaller oscillations inbetween at lower q , due to core/shell interferences. The remarkably small polydispersity of the particles and the respective superlayer thickness ($\sigma_R = 0.03$) leads to the large number of form factor oscillations. The minimum q -value of the instrumental setup is indicated.

space group of the lattice (see Tables 2, 3, and 4). Different crystalline lattices have different relative positions of the higher order reflections. The peak width of the reflections is reciprocally related to the domain size of the ordered domain. The intensities of the higher-order reflections are damped due to deviations from the ideal lattice positions (Debye–Waller factor) and are suppressed at specific q -values due to minima of the fluctuation term $\beta(q)$ (see Figure 2). The structure factor approaches $S(q) \rightarrow 1$ for $q \rightarrow \infty$ and $S(q) \rightarrow \infty$ for $q \rightarrow 0$.

Most of the structural variables discussed above, e.g., unit cell dimension and relative displacement, particle radius, and relative standard deviation, have a specific effect on the scattering curve, i.e., unit cell dimension a : position of the first reflection; lattice-type: relative position of higher-order reflections; root-mean-square displacement σ_a : damping of higher-order reflections; particle radius R : first minimum of oscillations; particle shape (sphere, cylinder, disk): relative position of higher order oscillations; particle polydispersity σ_R : damping of higher order oscillations; ordered domain size D : peak width; parameter ν : peak shape. This is favorable for the fitting of scattering curves to the expression of $I(q)$ in eq 30. Since each fit parameter has a specific effect on the scattering curve, this leads in most cases to low values of the off-diagonal elements of the covariance matrix, which indicates reasonable statistical independence.

Additional features in the scattering curve can arise in the case of core/shell particles, where additional oscillations from the particle shell and core/shell interference terms depending on the total radius R_m , shell/core scattering length ratio ρ , and the density profile scaling parameter α , can be observed. Furthermore, core/shell structures can lead to a suppression of the scattered intensity at intermediate q , when the contrast density of core and shell have opposite signs. This will be discussed below for SAXS curves of hexagonally packed cylinders in a lyotropic liquid crystalline phase.

4.2. Core/Shell Nanoparticles. Figure 8 shows the high q part of a synchrotron SAXS curve of Au@SiO₂ core/shell nanoparticles. The nanoparticles have a Au core with diameter

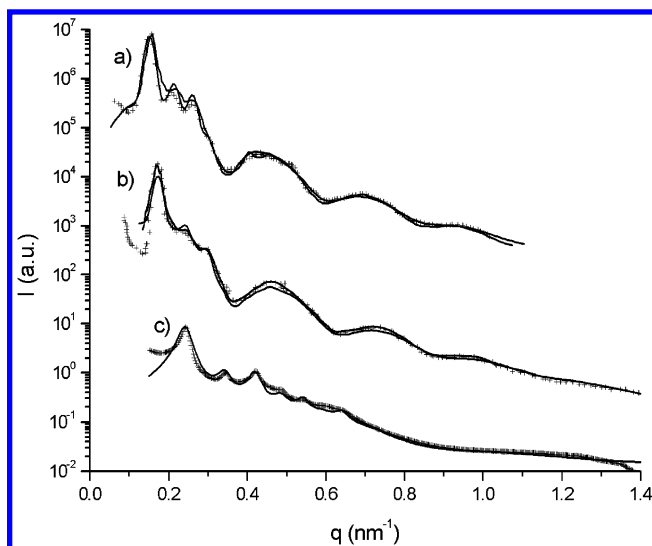


Figure 9. Comparison of measured and fitted SAXS curves for a PS–PI (a, ref 10; b, ref 36) and a lyotropic phase of PI–PEO-9 in methylcyclohexane (c). The gray lines are best fits to paracrystal theory (taken from 10 and 36). The black lines are fits to eq 30. The quality of the description for both models is well comparable. The fit parameters are summarized in Table 5.

15 nm and a thick SiO₂ shell with a total particle diameter of 75 nm. Interestingly, the nanoparticles assemble into layers giving rise to a scattering curve which can be nearly quantitatively described by a planar core/shell layer with a total diameter of $2R_m = 68.2$ nm, a core diameter of $2R_c = 13.7$ nm, and an electron density ratio of shell/core $\rho = 0.30$ with a nearly homogeneous shell ($\alpha = 0.042$). The large number of oscillations indicate that the polydispersity of the layer thickness is very low, i.e., $\sigma_R = 0.030$. The eight main oscillations are due to the high-density core of the layer. The sharp oscillations between the main oscillations at low q are due to core/shell interferences. This shows that eqs 18 and 19 give a good description of the form factor of core/shell structures. The arrangement of the nanoparticles into layers occurs as a consequence of the sample preparation (sol/gel reaction under centrifugation) and is further supported by scanning electron microscopy.²²

4.3. bcc Structures: Comparison to Paracrystal Theory.

Figure 9a shows the SAXS curve of a PS–PI block copolymer ($M_n = 21.9 \times 10^4$ g/mol, 15.4 wt % PI) where spherical PI domains are arranged on a *bcc* lattice.¹⁰ The first three reflections, (110), (200), and (211), are clearly observed, followed by three form factor oscillations at higher q . The oscillations can well be described yielding the radius and polydispersity of the PI spheres. The positions, intensities, widths, and shapes of the reflections are well captured by the fit to eq 30 (black line) and are comparable or even better than the description by paracrystal theory (gray line). The results of paracrystal theory and fits to eq 30 considering particle radius, standard deviation, mean deviation, and unit cell dimensions are the same within experimental error and are summarized in Table 5.

Figure 9b shows a SAXS curve of another PS–PI block copolymer ($M_n = 17.6 \times 10^4$ g/mol, 15.0 wt % PI), where also in this case spherical PI domains are arranged on a *bcc* lattice.³⁶ The first three reflections are well observed, followed by three form factor oscillations at higher q . The gray line is the fit using paracrystal theory.³⁶ The data can also be well described by using eq 30 (black line), however, with a slightly poorer fit. The parameters for the paracrystal fit³⁶ and the parameters

TABLE 5: Figure and Reference, Lattice Type, Lattice Constant a , Particle (core) Radius \bar{R}_c , Relative Standard Deviation of Particle Radius (polydispersity) σ_R , Total Particle Radius R_m , Density Profile Exponent α , Shell/Core-Scattering Length Ratio ρ_i , Domain Size D , Mean Lattice Deviation $\Delta = \bar{a}\sigma_a$, Caillé Parameter η , Peak Shape Parameter ν and Calculated Volume Fraction ϕ for the Scattering Curves Shown in Figures 8–13, Compared to the Parameters Derived from Paracrystal and Caillé Models

Figure	8	9a	9a	9b	9b	9c	10a	10a	10b	10b	10c
sample	Au/SiO ₂	PS–PI	PS–PI	PS–PI	PS–PI	PI–PEO	DDAB	DDAB	AOT	AOT	PI–PEO
fit/ref	eq 30	eq 30	ref 10	eq 30	ref 36	eq 30	eq 30	ref 12	eq 30	ref 12	eq 30
lattice	-	BCC	BCC	BCC	BCC	BCC	Lam	Lam	Lam	Lam	Lam
a (nm)	-	57.8	56.7	51.5	48.9	36.58	52.96	-	8.25	-	29.07
\bar{R}_c (nm)	6.85	13.6	13.1	12.6	12.6	5.55	1.26	1.23	0.88	0.80	6.9
σ_R	0.03	0.091	0.1	0.091	0.079	0.141	0.132	-	0.213	-	0.084
R_m (nm)	34.1	-	-	-	-	13.56	-	-	-	-	-
α	0.042	-	-	-	-	0.11	-	-	-	-	-
ρ_i	0.300	-	-	-	-	0.066	-	-	-	-	-
D (nm)	-	492.3	-	533.2	-	192.8	205.1	-	42.16	-	254.8
Δ (nm)	-	5.21	5.67	6.17	4.23	3.11	7.254	-	1.43	-	1.3
η	-	-	-	-	-	-	0.16	0.16	0.26	0.25	0.016
ν	-	Gauss	-	Gauss	-	0.21	1.98	-	Gauss	-	0.087
ϕ	-	0.111	0.099	0.123	0.14	-	0.047	0.040	0.212	0.20	0.475

Figure	11	11	11	11	11	11	12a	12b	12c	12d	13a	13b
sample	5%	15%	25%	35%	45%	55%	40%	hybrid	SiO ₂	hybrid	PS–PI	PS–PI
fit/ref.	eq 30	eq 30	eq 30	eq 30	eq 30	eq 30	eq 30	eq 30	eq 30	eq 30	eq 27	eq 27
lattice	Hex	Hex	Hex	Hex	Hex	Hex	Hex	Hex	Hex	FCC	2D-Hex	2D-Hex
a (nm)	32.82	30.06	29.11	27.46	25.60	24.81	32.6	25.5	22.3	34.5	168.0	(780)
\bar{R}_c (nm)	6.75	6.60	6.78	6.82	7.12	7.33	8.44	8.30	7.33	9.62	65.6	48.3
σ_R	0.083	0.062	0.086	0.086	0.061	0.071	0.077	0.09	0.07	0.072	0.30	0.30
R_m (nm)	11.49	11.75	11.0	10.80	-	-	-	-	-	-	-	-
α	0.049	0.27	0.36	0.06	-	-	-	-	-	-	-	-
ρ_i	-0.373	-0.275	-0.308	-0.251	-	-	-	-	-	-	-	-
D (nm)	64.2	171.1	199.9	143.2	215.5	195.0	100.0	90	100	134.0	354.8	60.0
Δ (nm)	3.13	1.28	1.25	1.32	1.30	1.63	2.36	2.5	2.1	1.56	17.7	40.0
η	-	-	-	-	-	-	-	-	-	-	-	-
ν	55.1	1.32	0.56	0.30	0.37	0.76	Gauss	0.38	0.39	Gauss	Gauss	Lorentz
ϕ	-	-	-	-	-	-	0.243	0.384	0.392	0.362	-	-

obtained from the fit to eq 30 are the same within experimental error and are summarized in Table 5.

Figure 9c shows a synchrotron SAXS curve of an inverse micellar phase of PI–PEO-2 in methylcyclohexane where PEO micelles are arranged on a *bcc* lattice. The first seven reflections [(110), (200), (211), (220), (310), (222), and (321)] are well observed. The damped oscillation due to the form factor can be well described, as are the positions, intensities, widths, and shapes of the peaks. The fit parameters are summarized in Table 5. The deviations at low q , where the experimental scattering curve increases whereas the calculated curves decrease, are due to structural features on length scales $d > 2\pi/q$, which are not included in the current model.

4.4. Lamellar Structures: Comparison to Caillé Theory.

Figure 10 shows SANS curves of two bilayer-forming surfactant systems: (a) DDAB/D₂O at a volume fraction of $\phi = 0.04$, and (b) AOT/D₂O at a volume fraction of $\phi = 0.20$. In the first case, the first three and in the latter case the first two reflections of the arrangement of bilayers are visible. For curve (a) at higher q there is a strong decay with an oscillation at $q \approx 0.2$ – 0.3 nm⁻¹ characteristic for the local bilayer structures. Peak intensities, shapes, positions, and widths can be well described by eq 30. The fitted curve (black line) compares well with the data and the description by the Caillé model (gray line); at low q the description with eq 30 is even better. Fit parameters such as bilayer thickness, unit cell dimension, and Caillé parameters are summarized in Table 5. The Caillé parameters calculated with eq 26 are $\eta = 0.26$ for AOT/D₂O and $\eta = 0.15$ for the DDAB/D₂O system, which compare well with the values obtained by Nallet et al., which is $\eta = 0.25$ and $\eta = 0.16$, respectively. Also the bilayer thicknesses of 1.75 for AOT and 2.52 nm for DDAB are in good agreement with the values determined using the Caillé model, being 1.60 and 2.46 nm.¹²

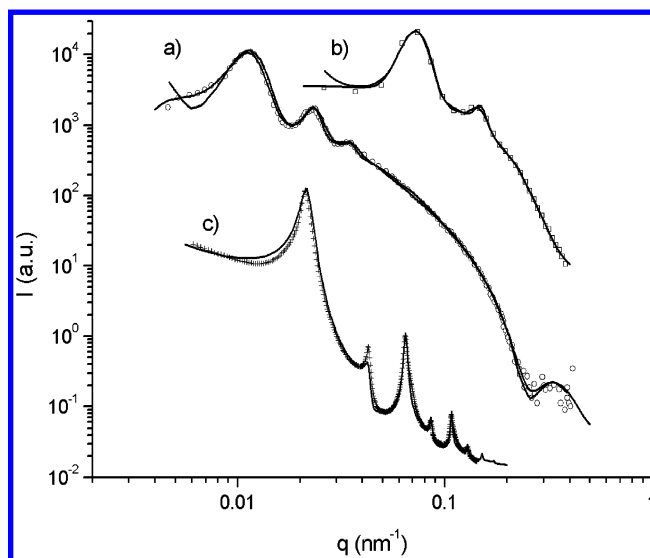


Figure 10. Comparison of measured and fitted SANS curves for lamellar phases of DDAB/D₂O (a) and AOT/D₂O (b) (both data taken from ref 12), together with a SAXS curve of a lamellar lyotropic phase of PI–PEO-3H₂O (70 wt %) (c). The calculated scattering curves obtained by the Caillé model (gray lines, taken from ref 12) and fits to eq 30 (black lines) are also shown. The quality of the description for both models is well comparable. The fit parameters are summarized in Table 5.

Figure 10c shows a synchrotron SAXS curve obtained from a lamellar lyotropic liquid crystal of a poly(isoprene-*b*-ethyleneoxide) (PI–PEO) block copolymer at a concentration of 60 wt % in water. The scattering curve shows the first six reflections whose position, intensity, width, and shape can be well described. The parameters obtained from the fitted curve (black line) are summarized in Table 5.

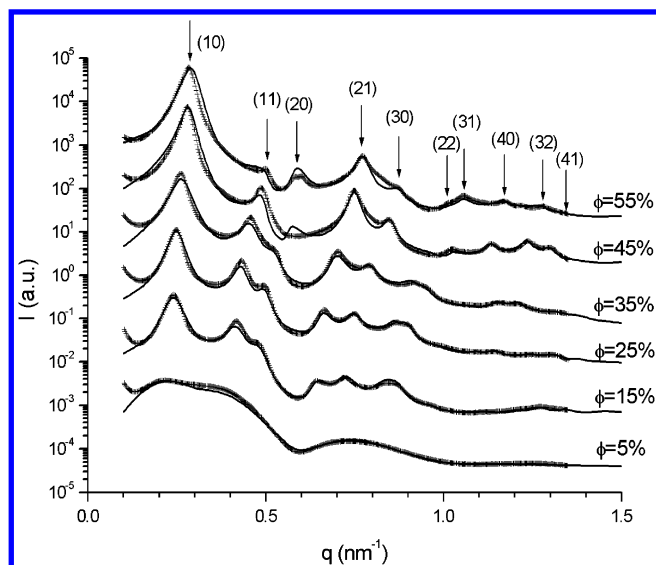


Figure 11. Comparison of measured and fitted synchrotron SAXS curves of block copolymer lyotropic liquid crystals (PB-PEO-16, hexagonal phase) for polymer concentrations of 5, 15, 25, 35, 45, and 55%. Over the complete concentration range the scattering curves can be well described by using eq 30. The fit parameters are summarized in Table 5.

4.5. Hexagonal Lyotropic Phases. Figure 11 shows a series of synchrotron SAXS curves of poly(butadiene-*b*-ethyleneoxide) (PB-PEO-16) in water, where the block copolymer forms cylindrical micelles. At the lowest concentration (5 wt % polymer) the scattering curve is dominated by the form factor exhibiting two oscillations, with a slight suppression of the scattering intensity at low q due to short-range intermicellar correlations. For concentrations of 15 wt % and above, the scattering intensity is dominated by the structure factor of the hexagonal liquid crystalline phase. The intensity is considerably suppressed at $q \approx 0.6 \text{ nm}^{-1}$ and $q \approx 1.0 \text{ nm}^{-1}$ due to the minima of the form factor. With increasing concentration, the peaks are systematically shifted to higher q values and higher order peaks become more intense. The scattering curves with the positions, intensities, and widths of the reflections can be well described and fitted (solid lines). The fit parameters are summarized in Table 5. Some deviations are observed around the (20)-reflections for the two highest concentration, whose origins are currently not yet clear. Also, the shape of the intense first reflection at the highest concentration cannot be quantitatively described. However, other peak shape functions (modified Lorentzian 1 and 2, pseudo-Voigt, Pearson VII) gave even worse agreement with the experimental data.

The fit parameters, given in Table 5, allow one to follow details of the structural evolution of the hexagonal phase with increasing polymer concentration. As expected, the unit cell dimension decreases with increasing concentration, but it is also observed that the core radius R of the cylindrical micelles significantly increases (from 6.7 to 7.3 nm) and that the size distribution becomes narrower (from 10% to 7% relative standard deviation). The PEO shells of the cylindrical micelles contribute notably to the scattered intensity at lower concentrations. Since micellar core and shell have lower and higher scattering length densities with respect to water, this leads to a negative ratio ρ (see Table 5) with a notable damping of the scattered intensity in the low q region. This effect is seen from the smaller intensity ratio of the first- to second-order peak at lower polymer concentrations.

4.6. Nanohybrid and Mesoporous Structures. Figure 12 shows SAXS curves measured with a rotating anode for the

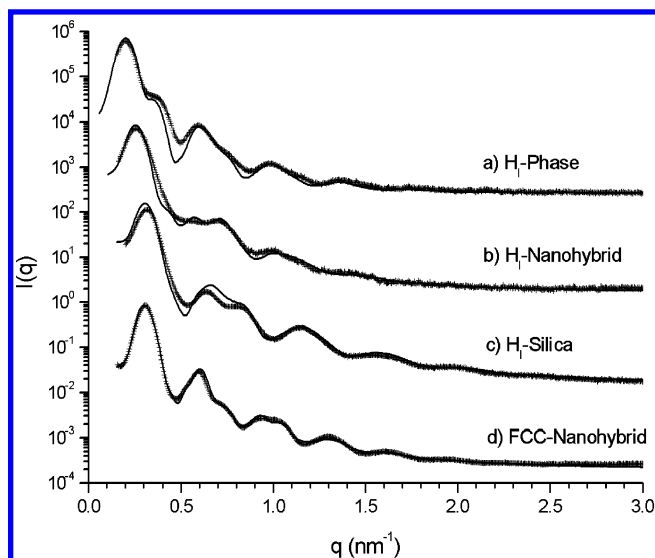


Figure 12. Comparison of measured and fitted SAXS curves for a hexagonal lyotropic phase of PI-PEO-11 (a), the corresponding polymer/silica hybrid (b), and the mesoporous silica (c) prepared therefrom. Also shown is the SAXS curve of a fcc-polymer/silica hybrid (d) prepared from an fcc-lyotropic block copolymer phase. Solid lines are fits to eq 30 with the fit parameters given in Table 5.

different stages of a sol/gel process that leads to the formation of an ordered mesoporous material from a lyotropic hexagonal phase. In this process, a silicic acid precursor, tetramethoxysilane (TMOS), is hydrolyzed and condensed in the aqueous domain of the hexagonal phase (Figure 12a) to obtain an ordered polymer/silica nanohybrid material (Figure 12b).^{1,2} The polymer is then removed by calcination to obtain the corresponding mesoporous material (Figure 12c). The scattering curves show peaks corresponding to the expected hexagonal packing and oscillations due to the form factor of the cylindrical micelles. The hexagonal order is preserved during the sol/gel process. Only the unit cell dimension is decreasing (32.6→25.5→22.3 nm), as is the diameter of the PI cylindrical core, which later becomes the mesopore (8.44→8.30→7.33 nm). The calcination leads to a nearly affine shrinking of unit cell dimension and pore diameter. From the volume fraction $\phi = 0.392$ (Table 5) and the density of amorphous silica, $\rho_{\text{SiO}_2} = 2.1 \text{ g/cm}^3$, the specific surface area of the material can be calculated (eq 38) i.e., $A_{\text{SiO}_2} = 83.8 \text{ m}^2/\text{g}$. This is a rather small value. Experimentally determined values using nitrogen adsorption often yield values that are of the order of several hundred m^2/g , indicating the presence of a considerable amount of microporosity in such samples.³⁷

Also shown is an SAXS curve (Figure 12d) measured with a rotating anode of a polymer/silica nanohybrid material prepared from the fcc phase of a PEB-PEO block copolymer in water. The first two reflections of the fcc lattice are not resolved, so that the (200) reflection appears as a shoulder on the (111) reflection. Similarly, the (220), (222), and (311) reflections are smeared out to the second broad peak. Still, the peaks and oscillations can be quantitatively described by eq 30. The fit parameters are given in Table 5.

Deviations between calculated and measured scattering curves are most prominent in the q -range around the first minimum of the form factor. In this q range, effects of both form factor and structure factor interfere, and the calculated scattered intensity critically depends on the peak shape function and the particle size distribution function. A better description would involve the consideration of defect structures, as well as higher moments

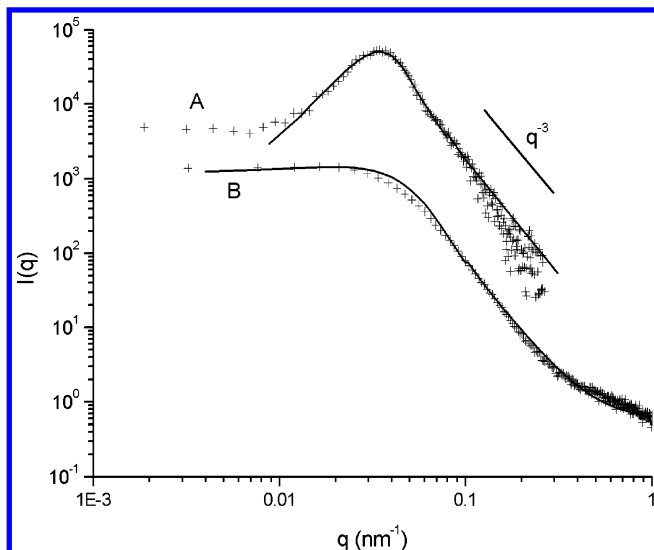


Figure 13. GISAXS out-of-plane scans for a thin (A) and a thick (B) PS-PI block copolymer film (data taken from ref 34). Solid lines are fits using eq 30 with the 2D form factor of eq 32.

of the lattice site and particle size distribution of such materials. Another extension of the model, which is being developed, is the consideration of orientation order that can be modeled by appropriate orientational distribution functions.³⁸

4.7. Mesoscopically Structured Thin Films. Figure 13 shows out-of-plane scans of GISAXS patterns measured for a thin (a) and thick (b) poly(styrene-*b*-isoprene) (PS-PI) block copolymer film, which had been spin-coated on top of an oxide-covered Si substrate.³⁴ These scans probe lateral structures in the film plane. The strong peak in Figure 13a indicates a regular two-dimensional distribution of domains within the film. The fit yields an interdomain distance of 168 nm with domain radii of 65.6. The GISAXS out-of-plane scan of the corresponding thick PS-PI film (Figure 13b) shows no clear peak, indicating poor order, with the domains having radii of 48.3 nm. The solid lines in Figure 13 are fits to eq 30 using the 2D form factor (eq 32), which shows the expected q^{-3} scaling.

Equations 30 and 32 also allow to calculate the complete two-dimensional diffuse scattering pattern of the thin film assuming cylinders of a length of $L = 100$ nm and polydispersity $\sigma_L = 0.3$ (Figure 14a). This pattern compares well with the diffuse

part of the experimentally determined GISAXS pattern.³⁴ Figure 14b shows the calculated diffuse scattering pattern for the same cylinders with narrow disperse cross-sections and lengths, i.e., $\sigma_R = 0.05$ and $\sigma_L = 0.05$ to illustrate the periodic oscillations due to the cylinder form factor.

5. Conclusions

We have outlined a general and versatile method that yields analytical expressions for the scattering curves of spheres, cylinders, and lamellae arranged on different lattices. This allows one to quantitatively fit experimentally measured SAXS and SANS curves of lipid and block copolymer liquid crystalline phases, as well as of core/shell nanoparticle superstructures, ordered nanocomposites, and mesoporous materials. For spheres arranged in cubic lattices, the description of the scattering curves compares with the paracrystal model. For lamellae or bilayers, there is good agreement with the Caillé model. Thus, this method allows a fast and nearly complete analysis of scattering curves of mesoscopically ordered materials. The outlined method can be easily extended to describe the diffusive part of out-of-plane scans of GISAXS and GISANS experiments on mesoscopically ordered thin films.

Acknowledgment. We thank P. Müller-Buschbaum for providing the original GISAXS data sets and N. Freiberger and O. Glatter for helpful suggestions. Financial support of the SFB 508 “quantum materials” is gratefully acknowledged.

Appendix

Hypergeometric Functions. The hypergeometric functions ${}_pF_Q$ can be written in terms of series expansions

$${}_pF_Q[a_1, \dots, a_p, b_1, \dots, b_Q; x] = \sum_{n=0}^{\infty} \frac{(a_1)_n (a_2)_n \dots (a_p)_n}{(b_1)_n (b_2)_n \dots (b_Q)_n} \frac{x^n}{n!} \quad (\text{A1})$$

where $(c)_n$ are the Pochhammer factorials given by

$$(c)_n = \frac{\Gamma(c+n)}{\Gamma(c)} = c(c+1)(c+2)\dots(c+n-1) \quad (\text{A2})$$

In the derivation of the scattering functions, the hypergeometric

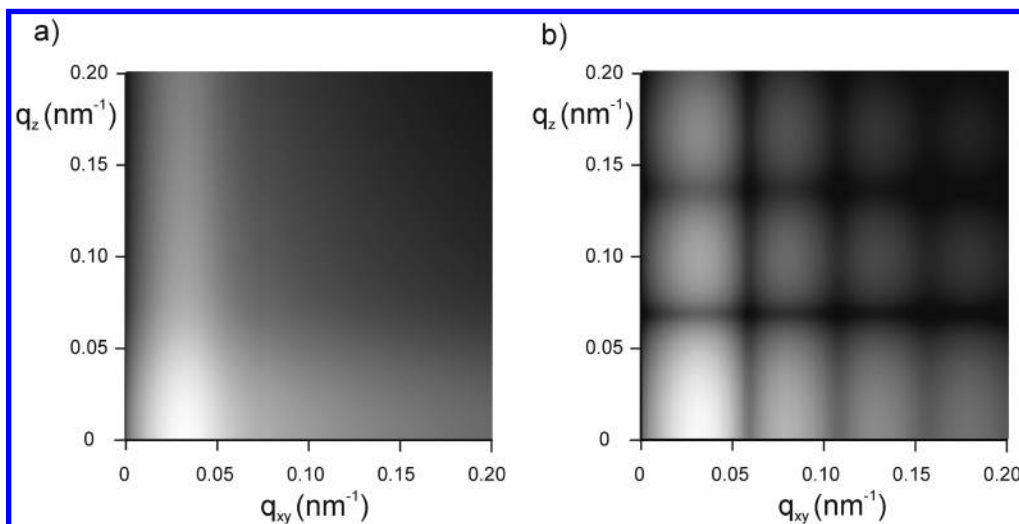


Figure 14. (a) Calculated two-dimensional diffuse scattering (GISAXS) for a thin PS-PI block copolymer film (Figure 13a) using the fit parameters given in Table 5 and assuming a cylinder length of $L = 100$ nm with $\sigma_L = 0.30$. For comparison, the corresponding scattering pattern for narrow disperse cylinders ($\sigma_R = 0.05$, $\sigma_L = 0.05$) is shown in (b) to illustrate the periodic oscillations due to the form factor of the cylinders.

functions ${}_0F_1[b_1; x]$ (eqs 4, 6), ${}_1F_2[a_1, b_1, b_2; x]$ (eqs 5, 7, 20), ${}_2F_1[a_1, a_2, b_1; x]$ (eqs 12, 14), and ${}_3F_2[a_1, a_2, a_3, b_1, b_2; x]$ (eqs 13, 15, 22) had been considered. In cases where the hypergeometric functions reduce to simpler functions, these have been compiled in Table 1. The sums in eq A1 can be easily calculated via the recurrence relation of the Pochhammer factorial $(c)_{n+1} = (c+n)(c)_n$. This enables an efficient implementation of these functions in fitting algorithms.

In cases where the hypergeometric function reduces to simple trigonometric functions (see Table 1), the expressions for $\langle F_{d\perp}(q) \rangle$ and $\langle F_{d\perp}^2(q) \rangle$ involve averages for the Schulz–Zimm distribution which are given by¹⁷

$$\langle x^{2n} \rangle = \frac{\Gamma[z+2n+1]}{\Gamma[z+1]} u^{2n} = \left(\frac{z+1}{2} \right)_n \left(\frac{z+2}{2} \right)_n (2u)^{2n} \quad (\text{A3})$$

$$\langle \sin(ax)x^n \rangle = \frac{\Gamma[z+n+2]}{\Gamma[z+1](z+n+1)} u^n \frac{\sin[(z+n+1)\arctan(au)]}{(1+a^2u^2)^{(z+n+1)/2}} \quad (\text{A4})$$

$$\langle \cos(ax)x^n \rangle = \frac{\Gamma[z+n+1]}{\Gamma[z+1]} u^n \frac{\cos[(z+n+1)\arctan(au)]}{(1+a^2u^2)^{(z+n+1)/2}} \quad (\text{A5})$$

$$\langle \sin^2(ax)x^n \rangle = \frac{\Gamma[z+n+3]}{\Gamma[z+1](z+n+1)(z+n+2)} \frac{u^n}{2} \times \left(1 - \frac{\cos[(z+n+1)\arctan(2au)]}{(1+4a^2u^2)^{(z+n+1)/2}} \right) \quad (\text{A6})$$

$$\langle \cos^2(ax)x^n \rangle = \frac{\Gamma[z+n+1]}{\Gamma[z+1]} \frac{u^n}{2} \times \left(1 + \frac{\cos[(z+n+1)\arctan(2au)]}{(1+4a^2u^2)^{(z+n+1)/2}} \right) \quad (\text{A7})$$

$$\langle \sin(ax)\cos(ax)x^n \rangle = \frac{\Gamma[z+n+2]}{\Gamma[z+1](z+n+1)} \frac{u^n}{2} \frac{\sin[(z+n+1)\arctan(2au)]}{(1+4a^2u^2)^{(z+n+1)/2}} \quad (\text{A8})$$

with $u = \bar{x}/(z+1)$. For $d = 3$, the expression for $\langle F_{d\perp}(q) \rangle$ has previously been derived in ref 23 and for $\langle F_{d\perp}^2(q) \rangle$ in ref 39.

For the average $\langle x^{2n} \rangle$, the relation in terms of Pochhammer factorials as given in eq A3 leads to the general relation

$$\langle {}_pF_Q[a_1, \dots, a_p, b_1, \dots, b_Q; -x^2] \rangle = {}_{p+2}F_Q\left[a_1, \dots, a_p, \frac{z+1}{2}, \frac{z+2}{2}, b_1, \dots, b_Q; (-2u)^2\right] \quad (\text{A9})$$

which has been used to derive eqs 12, 13, 14, 15, and 22.

Analytic Continuation and Asymptotic Expansion. For large q , the summation in eq A1 can break down due to rounding errors. In this case the hypergeometric functions can be calculated via analytic continuations or asymptotic expansions. For ${}_2F_1[a_1, a_2, b_1; x]$ in eqs 10 and 14, the following analytic continuations can be readily applied

$$\begin{aligned} {}_2F_1[a_1, a_2, b_1; x] &= (1-x)^{-a_1} {}_2F_1\left[a_1, b_1 - a_2, b_2; \frac{x}{x-1}\right] \\ &= (1-x)^{-a_2} {}_2F_1\left[a_2, b_1 - a_1, b_1; \frac{x}{x-1}\right] \end{aligned} \quad (\text{A10})$$

All scattering amplitudes $\langle F_{d\perp}(q) \rangle$ and $\langle F_{d\perp}^2(q) \rangle$ can be expressed in terms of the hypergeometric function ${}_1F_2[a_1, b_1, b_2; x]$,

e.g., for solid particles as the integrand in eqs 12 and 14 and the squared integrand in eqs 13 and 15, with $\alpha = 0$, as well as for core/shell particles and in eq 19. For this function, a quickly converging asymptotic expansion is

$$\begin{aligned} {}_1F_2\left[a_1, b_1, b_2; -\frac{x^2}{4}\right] &= \frac{\Gamma[b_1]\Gamma[b_2]}{\Gamma[a_1]} \pi^{-1/2} \left(\frac{x}{2}\right)^{s_1+1/2} \sum_{i=0}^{n_{\max}} c_i \cos\left[x + \frac{\pi}{2}\left(s_1 + \frac{1}{2} + n\right)\right] x^{-n} + \\ &\quad \frac{\Gamma[b_1]\Gamma[b_2]}{\Gamma[b_1-a_1]\Gamma[b_2-a_1]} \left(\frac{x^2}{4}\right)^{-a_1} \sum_{m=0}^{m_{\max}} d_m \left(-\frac{x^2}{4}\right)^{-m} \end{aligned} \quad (\text{A11})$$

with

$$d_m = \frac{(a_1)_m (1+a_1-b_1)_m (1+a_1-b_2)_m}{m!}$$

Here, $m_{\max} = 1$ and $n_{\max} = 2$ for sufficient accuracy. The first two terms of d_m are $d_0 = 1$ and $d_1 = a_1(1+a_1-b_1)(1+a_1-b_2)$. The other constants are given as

$$c_0 = 1$$

$$c_1 = \frac{1}{2} \left\{ \frac{1}{3} + s_1 - \left(s_1 + \frac{1}{2}\right)^2 - 2\left(-\frac{1}{3} - s_1 + s_2\right) \right\}$$

$$c_2 = \frac{(2c_1)^2}{8} + \frac{1}{6} \left\{ \frac{3}{2} \left(s_1 + \frac{1}{2}\right)^2 - \left(s_1 + \frac{1}{2}\right)^3 - \frac{1}{2} \left(s_1 + \frac{1}{2}\right) + 4\left(\frac{s_1}{2} - \frac{3s_2}{2} + s_3\right) \right\}$$

$$s_1 = a_1 - b_1 - b_2$$

$$s_2 = a_1^2 - b_1^2 - b_2^2$$

$$s_3 = a_1^3 - b_1^3 - b_2^3$$

The averages over the $\langle x^n \rangle$ and $\langle \cos(ax)x^n \rangle$ are given in eqs A3 and A5. The asymptotic behavior is discussed in ref 17. By changing from the series expansion (A1) to the asymptotic expansion (A11) at intermediate q , one calculates the function over the entire q -range.

Peak Shape Function. The peak shape function $L(q)$ (eq 27) is related to the Gamma function $\Gamma[z]$ as

$$L_{hkl}(q) = \frac{2}{\pi\delta} \prod_{n=0}^{\infty} \left(1 + \frac{\gamma_n^2 y^2}{(n+\nu/2)^2} \right)^{-1} = \frac{2}{\pi\delta} \left| \frac{\Gamma[\nu/2 + i\gamma_n y]}{\Gamma[\nu/2]} \right|^2 \quad (\text{A12})$$

with $y = 4(q - q_{hkl})^2/\pi^2\delta^2$. For $\nu < 0.001$ this function is practically equal to a Lorentzian, for $\nu > 1000$ practically equal to a Gaussian. For $\nu < 1$, the product converges quickly and a number of $n_{\max} \approx 20$ products is sufficient for high accuracy. For $\nu > 1$, convergence becomes slower and values of $n_{\max} \rightarrow 10^3$ are necessary, until for $\nu > 1000$ the Gaussian function becomes an excellent approximation.

References and Notes

- (1) Förster, S.; Plantenberg, T. *Angew. Chem., Int. Ed.* **2002**, *41*, 688.
- (2) Ying, J. Y.; Mehnert, C. P.; Wong, M. S. *Angew. Chem., Int. Ed.* **1999**, *38*, 56.
- (3) Seddon, J. M. *Biochim. Biophys. Acta* **1990**, *41*, 525.

- (4) Bleasdale, T. A.; Tiddy, G. J. T. In *The Structure, Dynamics and Equilibrium Properties of Colloidal Systems*; Bloor, D. M.; Wyn-Jones, E.:Eds.; Kluwer Academic: New York, 1990.
- (5) Percus, J. K.; Yevick, G. J. *Phys. Rev.* **1958**, *110*, 1.
- (6) Hayter, J. B.; Penfold, J. *Mol. Phys.* **1981**, *42*, 109.
- (7) Hansen, J. P.; Hayter, J. B. *Mol. Phys.* **1982**, *46*, 651.
- (8) Baxter, R. J. *J. Chem. Phys.* **1968**, *49*, 2770.
- (9) Matsuoka, H.; Tanaka, H.; Hashimoto, T.; Ise, N. *Phys. Rev. B* **1987**, *36*, 1754.
- (10) Matsuoka, H.; Tanaka, H.; Iizuka, N.; Hashimoto, T.; Ise, N. *Phys. Rev. B* **1990**, *41*, 3854.
- (11) Stribeck, N.; Ruland, W. *J. Appl. Crystallogr.* **1978**, *11*, 535.
- (12) Nallet, F.; Laversanne, R.; Roux, D. *J. Phys. II (France)* **1993**, *3*, 487.
- (13) Fröba, G.; Kalus, J. *J. Phys. Chem.* **1995**, *99*, 14450.
- (14) Pabst, G.; Rappolt, M.; Amenitsch, H.; Lagner, P. *Phys. Rev. E* **2000**, *62*, 4000.
- (15) Ruland, W.; Lecture on Polymer Physics, University of Marburg 1990.
- (16) Wolff, T.; Ph.D. Thesis, University of Marburg 1994.
- (17) Förster, S.; Burger, C. *Macromolecules* **1998**, *31*, 879.
- (18) Förster, S.; Krämer, E. *Macromolecules* **1999**, *32*, 2783.
- (19) Schellbach, C.; Diploma Thesis, University of Hamburg, 2003.
- (20) Förster, S. *Top. Curr. Chem.* **2003**, *226*, 1.
- (21) Lizmarzan, L. M.; Giersig, M.; Mulvaney, P. *Langmuir* **1996**, *12*, 4329.
- (22) Nakamura, H.; Förster, S.; Knott, R.; Mulvaney, P.; in preparation.
- (23) Kotlarchyk, M.; Chen, S.-H. *J. Chem. Phys.* **1983**, *79*, 2461.
- (24) Weyerich, B.; Brunner-Popela, J.; Glatter, O. *J. Appl. Crystallogr.* **1999**, *32*, 197.
- (25) *Higher Transcendental Functions*; Erdelyi, A., Ed.; Krieger: Florida, 1981; Vol. I.
- (26) Halperin, A.; Tirrell, M.; Lodge, T. P. *Adv. Polym. Sci.* **1992**, *31*, 100.
- (27) Förster, S.; Wenz, E.; Lindner, P. *Phys. Rev. Lett.* **1996**, *77*, 95.
- (28) Inouye, H.; Kirschner, D. A. *Fibre Diffr. Rev.* **2003**, *11*, 102.
- (29) Caillé, A. C. R. *Acad. Sci. Paris* **1972**, *B274*, 891.
- (30) Roux, D.; Safinya, C. R. *J. Phys. (France)* **1988**, *49*, 307.
- (31) *Fundamentals of Crystallography*; Giacovazzo, C., Ed.; Oxford: New York, 1992.
- (32) Micha, M. A.; Ph.D. Thesis, University of Potsdam, 1998.
- (33) Pedersen, J. S. *Adv. Colloid Interface Sci.* **1997**, *70*, 171.
- (34) Müller-Buschbaum, P. *Anal. Bioanal. Chem.* **2003**, *376*, 3.
- (35) Rauscher, M.; Salditt, T.; Spohn, H. *Phys. Rev. B* **1995**, *52*, 16855.
- (36) Iizuka, N.; Bodycomb, J.; Hasegawa, H.; Hashimoto, T. *Macromolecules* **1998**, *31*, 7256.
- (37) Göltner, C.; Smarsly, B.; Berton, B.; Antonietti, M. *Chem. Mater.* **2001**, *13*, 1617.
- (38) Förster, S.; Konrad, M.; Lindner, P. *Phys. Rev. Lett.*, in press.
- (39) Huang, J. S.; Sung, J.; Wu, X.-L. *J. Colloid Interface Sci.* **1989**, *132*, 34.